

Dipole-Bound State, Photodetachment Spectroscopy, and Resonant Photoelectron Imaging of Cryogenically-Cooled 2-Cyanopyrrolide

Published as part of *The Journal of Physical Chemistry virtual special issue "Paul L. Houston Festschrift"*.

Dao-Fu Yuan, Yue-Rou Zhang, and Lai-Sheng Wang*



Cite This: *J. Phys. Chem. A* 2022, 126, 6416–6428



Read Online

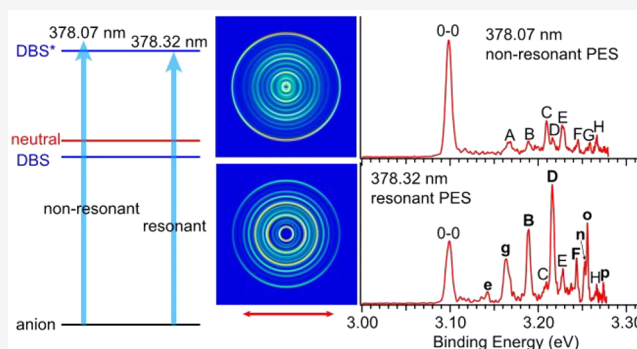
ACCESS |

Metrics & More

Article Recommendations

Supporting Information

ABSTRACT: Valence-bound anions with polar neutral cores can have diffuse dipole-bound excited states just below the electron detachment threshold. Because of the similarity in geometry and vibrational frequencies between the dipole-bound states (DBSs) and the corresponding neutrals, DBSs have been exploited as intermediate states to conduct resonant photoelectron spectroscopy (PES), resulting in highly non-Franck–Condon photoelectron spectra via vibrational autodetachment and providing much richer vibrational information than conventional PES. Here, we report a photodetachment and high-resolution photoelectron imaging study of the 2-cyanopyrrolide anion, cooled in a cryogenic ion trap. The electron affinity of the 2-cyanopyrrolyl radical is measured to be 3.0981 ± 0.0006 eV ($24\,988 \pm 5$ cm⁻¹). A DBS is observed for 2-cyanopyrrolide at 240 cm⁻¹ below its detachment threshold using photodetachment spectroscopy. Twenty-three above-threshold vibrational resonances (Feshbach resonances) of the DBS are observed. Resonant PES is conducted at each Feshbach resonance, yielding a wealth of vibrational information about the 2-cyanopyrrolyl radical. Resonant two-photon PES confirms the s-like dipole-bound orbital and reveals a relatively long lifetime of the bound zero-point level of the DBS. Fundamental frequencies for 19 vibrational modes (out of a total of 24) are obtained for the cyanopyrrolyl radical, including six out-of-plane modes. The current work provides important spectroscopic information about 2-cyanopyrrolyl, which should be valuable for the study of this radical in combustion or astronomical environments.



1. INTRODUCTION

Negatively charged ions usually have much smaller electron detachment energies relative to the ionization energies of neutral species and can rarely support bound excited electronic states.¹ However, anions with polar neutral cores of sufficiently large dipole moments can support a special class of excited electronic states just below the detachment threshold due to the charge-dipole interaction.^{2–14} The critical dipole moment to support such dipole-bound states (DBSs) was empirically determined to be around 2.5 D.^{15–18} DBSs are highly diffuse and weakly bound with binding energies on the order of a few to a few hundred cm⁻¹.^{1–23} Because the dipole-bound electron has little effect on the structure of the neutral core, the potential energy surface of the DBS is parallel to that of the neutral species with identical vibrational frequencies. Thus, vibrational excitations of the DBS can autodetach by coupling the vibrational energy to the dipole-bound electron with a propensity rule of $\Delta v = -1$.^{24,25}

Dipole-bound excited electronic states were first observed in photodetachment experiments to determine the electron affinities (EAs) of organic radicals^{2–4} and have allowed high-resolution photodetachment spectroscopy (PDS).^{5–8} By

tuning the detachment laser to a vibrational resonance (Feshbach resonance) of the DBS and dispersing the electron kinetic energy, one can conduct resonant photoelectron spectroscopy (rPES), which was first performed for cryogenically cooled phenoxide anions.¹⁰ It was found that vibrationally induced autodetachment was mode-specific, resulting in the enhancement of specific vibrational modes, in particular, for those with small or no Franck–Condon factors. In combination with cryogenic cooling of anions, DBSs have since been exploited as an important platform for obtaining vibrational information on radical species using rPES^{26–32} yielding much richer spectroscopic information than conventional PES. Pump–Probe experiments have also been utilized to investigate the autodetachment dynamics from the DBS.^{33,34}

Received: June 27, 2022

Revised: August 30, 2022

Published: September 13, 2022



Recently, we reported a high-resolution photoelectron imaging (PEI) and threshold photodetachment (PD) study of the pyrrolide anion ($C_4NH_4^-$).³⁵ However, we did not observe a DBS for pyrrolide because the dipole moment of the pyrrolyl radical (2.18 D) is below the critical dipole moment to support a DBS. Substituting one of the H atoms on the α -position by a CN group in pyrrolyl should significantly increase the dipole moment of the resulting 2-cyanopyrrolyl radical, making it possible for the 2-cyanopyrrolide anion (2-CNPyr⁻) to support a DBS. In this article, we report an investigation of cryogenically cooled 2-CNPyr⁻ using PDS and rPES and our observation of the DBS, allowing us to obtain fundamental frequencies for 19 vibrational modes (out of a total of 24) of the 2-CNPyr radical, whereas only eight vibrational frequencies (out of a total of 21) were obtained for the pyrrolyl radical in the recent PEI study.³⁵

Five-membered heterocyclic pyrroles and their derivatives have attracted broad interest because of their presence in many biologically important molecules.^{36,37} The pyrrole derivative, 2-cyanopyrrole, with a CN group in the α -position, is an important intermediate in the synthesis of porphyrins.³⁸ The 2-CNPyr⁻ anion is widely used in ionic liquids.³⁹ More significantly, CN-substituted molecules are of great interest in astrophysics. Both the CN radical and the CN⁻ anion have been detected in the interstellar medium (ISM).^{40–42} The CN radical has been shown to undergo barrierless reactions with organic molecules, conducive to the cold ISM environment, and it is believed to be one of the main sources of chemically active nitrogen-containing species.^{43–45} Several CN-substituted species have been discovered in the ISM, from the simple cyanomethyl radical (CH_2CN)^{46,47} to the CN-functionalized five- and six-membered ring molecules.^{48–51} Even though the 2-CNPyr radical and the 2-CNPyr⁻ anion have not been detected astronomically, laboratory spectroscopic data should provide important references for future observations.

Since the pioneering work by Chandler and Houston to image the photofragments of CH_3I ,⁵² the imaging technique has been extended to PEI,^{53,54} in particular, with the development of velocity-map imaging (VMI).⁵⁵ High-resolution PEI of negative ions has been championed by the Neumark group using slow electron velocity-map imaging (SEVI).⁵⁶ We have designed an experimental apparatus coupling electrospray ionization (ESI),⁵⁷ cryogenic ion cooling in a three-dimensional (3D) Paul trap,⁵⁸ and high-resolution PEI.⁵⁹ Using this third-generation ESI-PES apparatus,⁶⁰ we developed rPES using DBSs as the intermediate states and investigated a wide variety of cryogenically cooled anions,^{10,26–31} including several polycyclic aromatic hydrocarbon species.^{30,61–63} In this article, we present a study of the 2-CNPyr⁻ anion using PEI, PDS, and rPES. Nonresonant PES reveals strong vibronic couplings between the ground and the first excited electronic states of the 2-CNPyr radical. The EA of 2-CNPyr is measured to be 3.0981 ± 0.0006 eV ($24\,988 \pm 5$ cm⁻¹). A DBS is observed for 2-CNPyr⁻ with a binding energy of 240 ± 5 cm⁻¹ (0.0298 ± 0.0006 cm⁻¹), as well as 23 vibrational Feshbach resonances. The combination of high-resolution PEI, PDS, and rPES yields vibrational frequencies for 19 vibrational modes of the 2-CNPyr radical out of a total of 24 modes.

2. EXPERIMENTAL AND COMPUTATIONAL METHODS

2.1. Photoelectron Imaging. The experiment was carried out using our third-generation ESI-PES apparatus (Figure

S1)⁶⁰ equipped with a cryogenically cooled 3D Paul trap⁵⁸ and high-resolution photoelectron imaging.⁵⁹ The 2-CNPyr⁻ anion was produced by ESI of a 1 mM solution of 2-cyanopyrrole (Sigma-Aldrich, 96%) in a mixed solvent of CH_3OH/H_2O (9/1 ratio in volume) with several drops of a NaOH solution to enhance deprotonation. The 2-CNPyr⁻ anion generated in the ESI source was guided into a 3D Paul trap by a series of quadrupole and octupole ion guides. The ion trap is cryogenically cooled to 4.6 K using a closed-cycle helium refrigerator. After being accumulated for about 0.1 s and thermally cooled via collisions with a mixed background gas of He/H_2 (~ 1 mTorr, 4/1 in volume),⁵⁸ the anions were unloaded from the trap at a 10 Hz repetition rate and focused into the extraction zone of a modified Wiley–McLaren time-of-flight mass spectrometer. The 2-CNPyr⁻ anion was selected by a mass gate and photodetached in the interaction zone of a multilens VMI system⁵⁹ by a tunable dye laser or the fourth harmonic (266 nm) of an Nd:YAG laser. Photoelectrons were extracted from the interaction zone and projected onto a pair of 75 mm diameter microchannel plates coupled to a phosphor screen and captured by a charge-coupled-device camera. Photoelectron (PE) images were inverse-Abel transformed and reconstructed using the pBasex and BASEX programs.^{64,65} PE spectra were calibrated with the known spectra of Au^- at different photon energies. The kinetic energy (KE) resolution was 3.8 cm⁻¹ for electrons with 55 cm⁻¹ KE and about 1.5% ($\Delta KE/KE$) for KE above 1 eV in the current experiment. The resolution of PE images depends on the extraction voltage on the imaging lens. Lower extraction voltages give better resolution, but higher extraction voltages are needed for the detection of fast electrons. In the current experiment, the extraction voltage used was -300 V for all the PE images at photon energies below 3.5 eV and -700 V for the photon energy at 4.661 eV (266 nm). An even higher voltage (-1400 V) was required to detect the resonant two-photon detachment PE signals via the zero-point level of the DBS.

2.2. Photoelectron Angular Distributions. The differential detachment cross section for randomly oriented molecules with linearly polarized light can be expressed as⁶⁶

$$I(\theta) = \sigma_T/4\pi[1 + \beta P_2(\cos \theta)] \quad (1)$$

where σ_T is the total detachment cross section, β ($-1 < \beta < 2$) is the anisotropy parameter that describes the PE angular distribution (PAD), $P_2(\cos \theta)$ is the second-order Legendre polynomial, and θ is the angle between the ejected photoelectron and the polarization direction of the detachment laser. $\beta = 0$ results in an isotropic outgoing wave, while $\beta = -1$ gives rise to an (s + d) wave with the maximum intensity in the direction perpendicular to the laser polarization. $\beta = 2$ represents p-wave detachment with the maximum intensity along the laser polarization.

2.3. Computational Methods. Geometry optimization, ground-state electronic structure, and dipole moment calculations were performed using density functional theory (DFT) at the B3LYP/aug-cc-pVTZ level of theory. The electronic structure calculations were followed by vibrational analyses. All calculations were done using the Gaussian 09 package.⁶⁷

3. RESULTS

3.1. Nonresonant Photoelectron Imaging and Spectroscopy. The PE image and spectrum of 2-CNPyr⁻ at 266 nm are shown in Figure 1. A prominent band X at the low binding energy (BE) side is observed below ~ 3.6 eV,

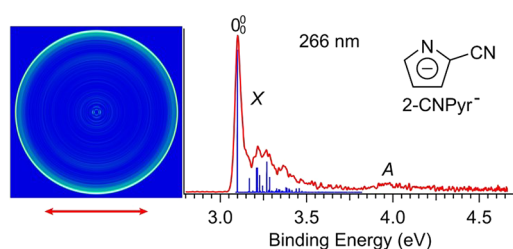


Figure 1. Photoelectron image and spectrum of 2-CNPyrr⁻ at 266 nm (4.661 eV). Calculated FC factors, given as vertical sticks, are shown for comparison. The calculated frequencies scaled by 0.972 (Table S1) are used in the FC simulation. (inset) The molecular structure of 2-CNPyrr⁻.

representing electron detachment from the highest occupied molecular orbital (HOMO) of the 2-CNPyrr⁻ anion (Figure 2).

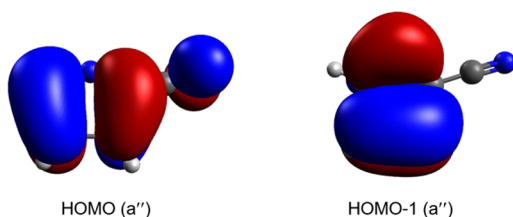


Figure 2. HOMO and HOMO-1 of 2-CNPyrr⁻ (isovalue = 0.02).

Band X display (s + d)-wave angular distributions with an average β value of -0.25 ± 0.05 , consistent with the π -type HOMO of 2-CNPyrr⁻. Peak 0_0^0 in band X denotes the detachment transition from the ground vibrational state of the 2-CNPyrr⁻ anion to that of the 2-CNPyrr neutral. The position of peak 0_0^0 at 3.10 eV defines the adiabatic detachment energy (ADE) of 2-CNPyrr⁻ or the EA of the 2-CNPyrr radical, which is much more accurately determined in the near-threshold spectra (vide infra). The calculated Franck–Condon (FC) factors are overlaid with the spectrum in Figure 1 as vertical lines for comparison, with the 0–0 transition aligned with peak 0_0^0 . The calculated frequencies at the B3LYP/aug-cc-pVTZ level of theory are scaled by a factor 0.972 (Table S1), based on the experimental values obtained in the high-resolution spectra (vide infra). Only in-plane vibrational transitions with A' symmetry are FC-active because of the C_s symmetry of both 2-CNPyrr⁻ and 2-CNPyrr. In addition to band X, another weak and featureless band A is observed around 4 eV in Figure 1, representing the electron detachment from the HOMO-1 of 2-CNPyrr⁻ (Figure 2) with the neutral in its first excited electronic state. Similarly, the PE image of band A also shows an (s + d)-wave distribution ($\beta = -0.60 \pm 0.05$), consistent with the π -type HOMO-1 of the 2-CNPyrr⁻ anion. The PE spectrum of 2-CNPyrr is similar to that of the parent pyrrolyl,³⁵ but the CN substitution increased the BE by about 1 eV.

To better resolve the vibrational features of the ground-state detachment transition, we have also taken three spectra at lower photon energies, as presented in Figure 3. The near-threshold spectrum at 399.77 nm (Figure 3a) gives a very sharp 0_0^0 peak, yielding an accurate EA of 3.0981 ± 0.0006 eV ($24\,988 \pm 5$ cm⁻¹) for the 2-CNPyrr radical. Numerous vibrational fine features, labeled as A–K, are resolved in the spectra at 378.07 nm (Figure 3b) and 373.47 nm (Figure 3c). The BEs of peaks A–K, which are determined more accurately

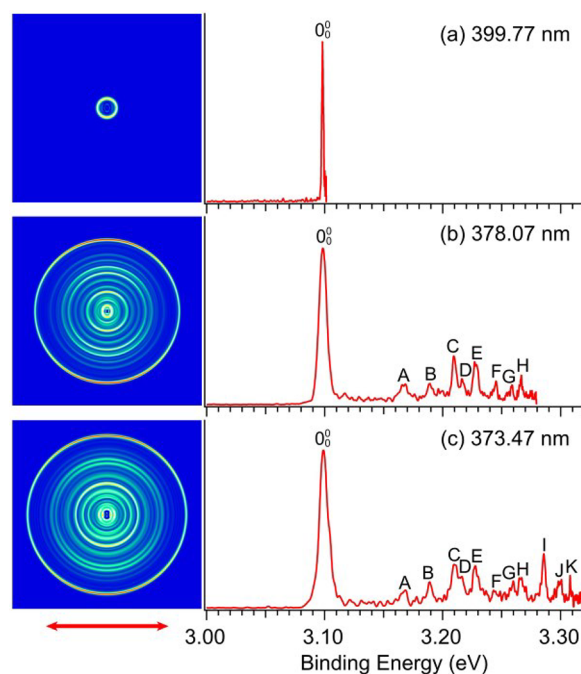


Figure 3. Nonresonant PE images and spectra of 2-CNPyrr⁻ at (a) 399.77 nm (3.1014 eV), (b) 378.07 nm (3.2794 eV), and (c) 373.47 nm (3.3198 eV). The observed peaks are labeled as 0_0^0 and A–K. The double arrow below the images represents the polarization direction of the detachment laser.

in rPES, and their assignments will be discussed along with the rPES (vide infra).

3.2. Photodetachment Spectroscopy. The CN group in 2-CNPyrr substantially increases its dipole moment to 4.8 D versus 2.18 D for the parent pyrrolyl, suggesting it should support a DBS as an excited electronic state of the 2-CNPyrr⁻ anion near its detachment threshold. To search for the expected DBS, PDS is conducted by scanning the laser wavelength across the detachment threshold and monitoring the total electron yield as a function of the photon energy, as shown in Figure 4. A step is observed promptly at the detachment threshold, coinciding with the EA accurately determined as $24\,988$ cm⁻¹ by the 0–0 transition in the near-threshold PE

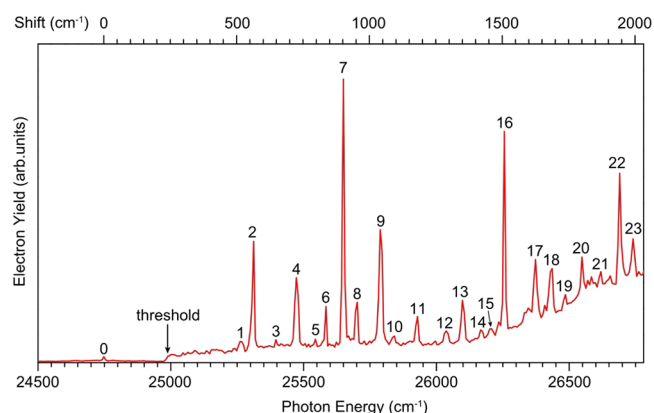


Figure 4. PD spectrum of 2-CNPyrr⁻ by measuring the total electron yield as a function of photon energy. The arrow indicates the detachment threshold. Vibrational Feshbach resonances of the DBS are labeled as 1–23.

spectrum (Figure 3a). The detachment cross section near threshold can be described well by the Wigner threshold law.⁶⁸ An $s + d$ wave is expected from detachment from the π HOMO of 2-CNPyr⁻; the step suggests that the s -wave dominates at the threshold. This behavior is very different from the PDS of pyrrolide, in which the d -wave dominates in the threshold and no step was observed.³⁵

The weak below-threshold peak 0 at 24 748 cm⁻¹ (3.0981 eV), observed due to resonant two-photon photodetachment (R2PD), indicates the existence of a DBS. It should correspond to the zero-point level of the DBS with a binding energy of 240 ± 5 cm⁻¹ (0.0298 ± 0.0006 eV) defined by its separation from the detachment threshold. Twenty-three above-threshold resonances (also known as (aka) vibrational Feshbach resonances) are observed in an energy range about 1800 cm⁻¹ above the threshold and they are labeled from 1 to 23. These resonances are due to excitations to vibrational levels of the DBS followed by vibrational autodetachment. The laser wavelengths, photon energies, and shifts to peak 0 of the 23 DBS vibrational peaks are presented in Table 1.

3.3. R2PD Photoelectron Imaging. By tuning the detachment laser wavelength to peak 0, that is, the zero-point level of the DBS, we obtained the R2PD PE image and spectrum, as shown in Figure 5. Two features are observed in the R2PD PE spectrum, labeled as “DBS” and “S₀”,

Table 1. Observed DBS Vibrational Peaks in the PD Spectrum of 2-CNPyr⁻, with Their Wavelengths, Photon Energies, Shifts Relative to the Ground Vibrational Level, and Assignments

peak	wavelength (nm)	photon energy (cm ⁻¹)	shift (cm ⁻¹)	assignment
0	404.07	24 748	0	ground state of DBS
1	395.85	25 262	514	16 ¹
2	395.07	25 312	564	15 ¹ /24 ¹ 23 ¹
3	393.81	25 393	645	21 ¹
4	392.55	25 474	726	14 ¹ /24 ¹ 23 ¹ 17 ¹
5	391.49	25 543	795	24 ¹ 21 ¹ /HB ^a
6	390.87	25 584	836	19 ¹ /23 ² /24 ¹ 22 ¹ 17 ¹
7	389.88	25 649	901	13 ¹
8	389.11	25 700	952	12 ¹ /23 ¹ 22 ¹
9	387.74	25 790	1042	11 ¹ /16 ² /22 ²
10	386.98	25 841	1093	10 ¹ /23 ¹ 22 ¹ 17 ¹
11	385.68	25 928	1180	9 ¹
12	384.03	26 040	1292	8 ¹ /21 ² /15 ¹ 14 ¹ /23 ¹ 13 ¹
13	383.18	26 097	1349	6 ¹ /17 ¹ 9 ¹
14	382.14	26 168	1420	16 ¹ 13 ¹
15	381.62	26 204	1456	15 ¹ 13 ¹ /23 ¹ 11 ¹ /14 ² /20 ²
16	380.86	26 256	1508	5 ¹ /15 ¹ 12 ¹ /22 ¹ 19 ¹ 17 ¹ /23 ² 17 ¹ 16 ¹
17	379.19	26 372	1624	14 ¹ 13 ¹ /16 ¹ 15 ² /23 ¹ 21 ¹ 15 ¹
18	378.32	26 433	1685	14 ¹ 12 ¹ /16 ¹ 9 ¹ /17 ² 7 ¹ /23 ¹ 20 ¹ 15 ¹
19	377.61	26 482	1734	23 ² 13 ¹ /15 ¹ 9 ¹
20	376.68	26 548	1800	13 ²
21	375.72	26 616	1868	16 ¹ 6 ¹ /17 ¹ 16 ¹ 9 ¹ /17 ² 5 ¹
22	374.67	26 690	1942	13 ¹ 11 ¹ /22 ² 13 ¹ /16 ² 13 ¹ /21 ¹ 20 ¹ 15 ¹
23	374.01	26 737	1989	13 ¹ 10 ¹ /12 ¹ 11 ¹ /16 ¹ 14 ² /20 ² 16 ¹ /21 ¹ 17 ¹ /23 ¹ 22 ³

^aHB denotes the contribution by a resonantly enhanced hot band.

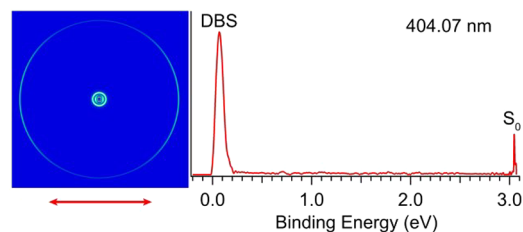


Figure 5. R2PD PE image and spectrum of 2-CNPyr⁻ at 404.07 nm (3.0684 eV) via the $\nu = 0$ level of the DBS, corresponding to peak 0 in Figure 4. The double arrow below the image represents the direction of laser polarization.

respectively. The strong DBS feature at the low BE side corresponds to R2PD, where the first photon excites the anion to the zero-point level of the DBS followed by detachment of the dipole-bound electron by a second photon within the same laser pulse. The very small binding energy of the DBS peak is consistent with the accurate measurement from the PD spectrum above. The distinct p -wave distribution with a β value of 1.40 ± 0.05 for the DBS feature confirms the s -like diffuse dipole-bound orbital. The weak sharp feature labeled as S₀ at the high BE side comes from electron signals detached from rovibrationally excited anions of the ground electronic state of 2-CNPyr⁻, populated by relaxations from the DBS after absorbing the first photon. This is a very weak signal, indicating the DBS is relatively long-lived.

3.4. Resonant Photoelectron Spectra of 2-CNPyr⁻ Via the Vibrational Feshbach Resonances. By tuning the wavelength of the detachment laser to the positions of the Feshbach resonances in Figure 4, we obtained 23 resonant PE spectra, as shown in Figure 6 for peaks 1–12 and Figure 7 for peaks 13–23. Since first realized for the phenoxide anion in 2013,¹⁰ rPES via DBS, enabled by cryogenic cooling of the anions,^{58,60} has been proved to be extremely powerful for obtaining spectroscopic information on neutral radical species than nonresonant PES.²⁶ Compared to the nonresonant PE spectra in Figure 3, one or more transitions are enhanced in the resonant spectra (labeled in bold face in Figures 6 and 7), and more interestingly new peaks appear (labeled as lowercase letters). The binding energies of all the peaks observed in the resonant and nonresonant PE spectra, their shifts relative to the 0–0 transition, and assignments are summarized in Table 2.

4. DISCUSSION

4.1. Nonresonant Photoelectron Spectra of 2-CNPyr⁻: Angular Distributions, Franck–Condon Simulations, and Vibrational Couplings. Twelve vibrational peaks (0₀⁰, A–K) are resolved in the nonresonant PE spectra (Figure 3), as summarized in Table 2. The PE images in Figure 3b,c exhibit ($s + d$)-wave angular distributions with the maximum intensity in the direction perpendicular to the laser polarization, consistent with the π HOMO of 2-CNPyr⁻ (Figure 2). The anisotropy parameter β of the 12 peaks observed in the spectrum at 373.47 nm (Figure 3c) are derived from the image and presented in Table 3, with the corresponding KE. The anisotropy parameter for the same detachment transition is usually KE-dependent. For example, peak 0₀⁰ in the near-threshold spectrum at 399.77 (3.1014 eV, Figure 3a) with a KE of 26 cm⁻¹ (0.0032 eV) is more isotropic ($\beta = -0.10 \pm 0.05$) than in the spectra with higher KE (Figures 1 and 3b,c). This

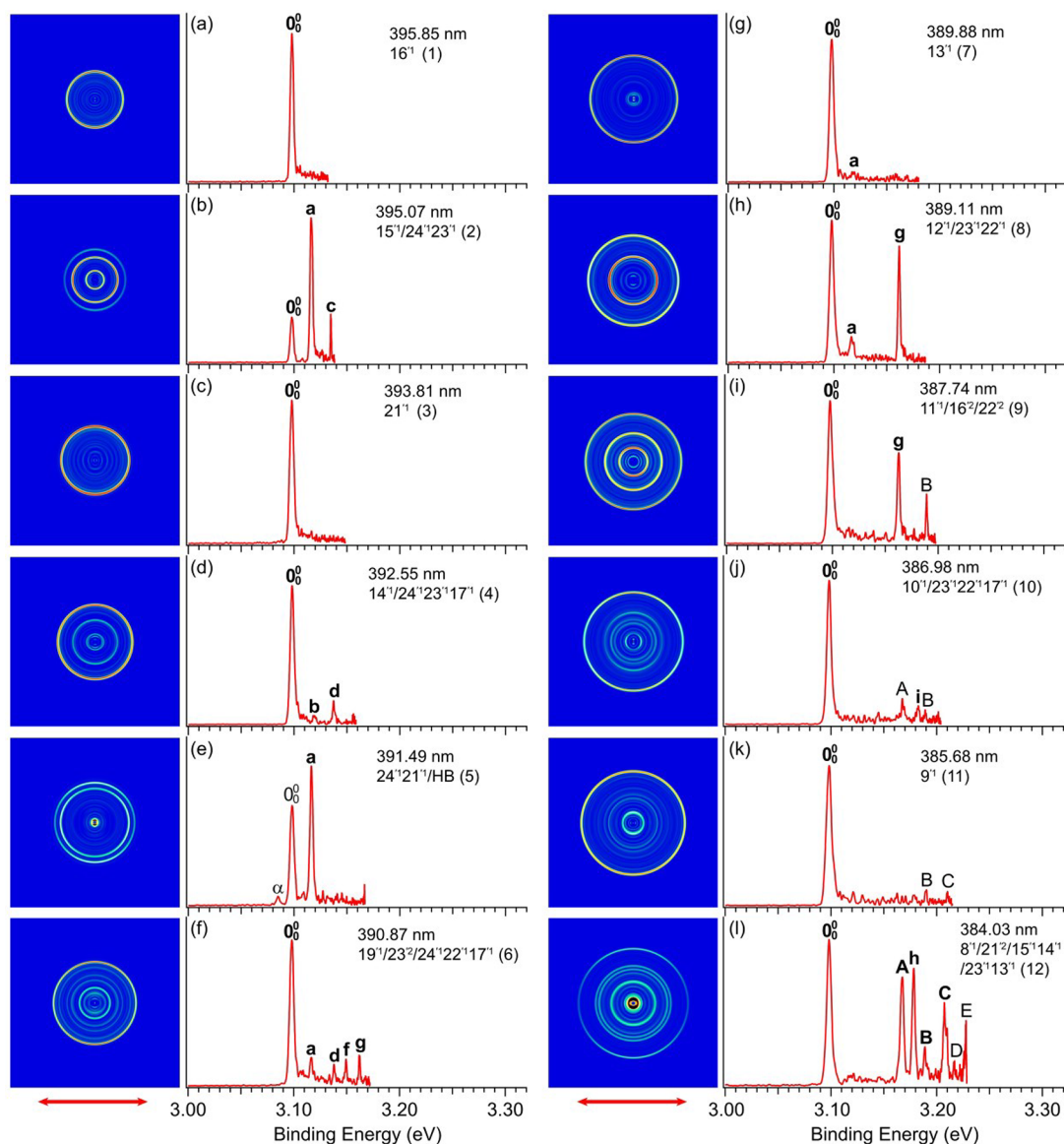


Figure 6. Resonant PE images and spectra of 2-CNPyr⁻ at the positions of peaks 1–12 in the PDS (Figure 4). (a) 395.85 nm (3.1321 eV), (b) 395.07 nm (3.1383 eV), (c) 393.81 nm (3.1483 eV), (d) 392.55 nm (3.1584 eV), (e) 391.49 nm (3.1670 eV), (f) 390.87 nm (3.1720 eV), (g) 389.88 nm (3.1801 eV), (h) 389.11 nm (3.1863 eV), (i) 387.74 nm (3.1976 eV), (j) 386.98 nm (3.2039 eV), (k) 385.68 nm (3.2147 eV), and (l) 384.03 nm (3.2285 eV). The double arrow below the image represents the direction of laser polarization.

observation is consistent with the threshold behavior revealed in the PD spectrum (Figure 4), which shows that the *s* partial wave is more dominant near threshold. It should be pointed out that this threshold behavior is completely different from that of the parent pyrroliide, which shows that the *d* partial wave is dominant near the threshold.³⁵ The π HOMOs of the two anions are similar, except that the HOMO of 2-CNPyr⁻ has some contribution from the CN group (Figure 2). The *d* wave dominance in pyrroliide made it very challenging to take high-resolution PE images near threshold because of the extremely low detachment threshold.³⁵

Since both 2-CNPyr⁻ and 2-CNPyr have planar structures with *C_s* symmetry, only the in-plane vibrational levels with *A'* symmetry are FC-allowed. The FC factors with the calculated frequencies at the B3LYP/aug-cc-pVTZ level of theory are compared with the nonresonant PE spectrum at 373.47 nm in Figure 8. All the FC peak positions agree well with the experimental data upon applying a scaling factor of 0.972 to

the computed frequencies. However, the magnitudes of the calculated FC factors for several vibrational peaks do not agree well with the observed peaks. For example, the FC factors for peaks B, J, and K are much weaker than the experimental peak heights, whereas the computed FC factor for peak G is negligible. Such non-FC behaviors indicate vibronic couplings between the ground state of the 2-CNPyr radical and its nearby excited states, which are known to be strong in the parent pyrrolyl radical.^{69,70} Another indication of the strong vibronic coupling is the negligible and unresolved band A in the 266 nm spectrum (Figure 1). This band represents the first excited state of 2-CNPyr, and it is similar to the behavior of the corresponding state in the parent pyrrolyl radical, for which sophisticated vibronic coupling calculations have been conducted.^{69,70} The behavior of band A is a direct consequence of strong vibronic coupling with the ground state. Thus, while most of the vibrational peaks observed in the PE spectra (Figure 3) can be assigned straightforwardly

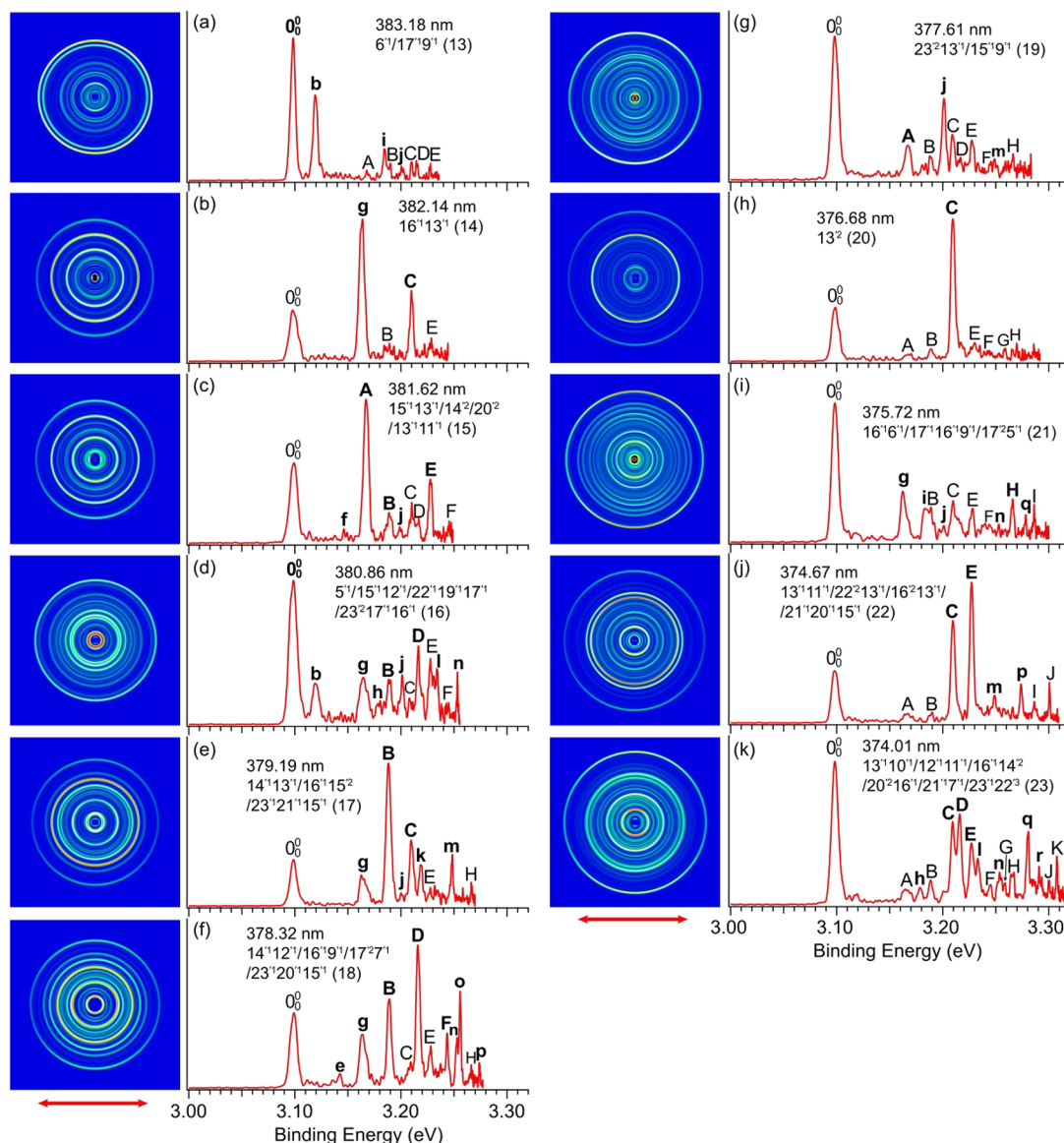


Figure 7. Resonant PE images and spectra of 2-CNPyrr⁻ at the positions of peaks 13–23 in the PDS (Figure 4). (a) 383.18 nm (3.2357 eV), (b) 382.14 nm (3.2445 eV), (c) 381.62 nm (3.2489 eV), (d) 380.86 nm (3.2554 eV), (e) 379.19 nm (3.2697 eV), (f) 378.32 nm (3.2772 eV), (g) 377.61 nm (3.2834 eV), (h) 376.68 nm (3.2915 eV), (i) 375.72 nm (3.2999 eV), (j) 374.67 nm (3.3092 eV), and (k) 374.01 nm (3.3150 eV). The double arrow below the image represents the direction of laser polarization.

according to the FC simulation (Table 2), the assignments of a few peaks, namely, B, G, J, and K, are confirmed from rPES to be discussed below. As shown in Table 2, peaks A–I are all due to the fundamental vibrational excitations of 2-CNPyrr⁻. The ν_{14} (A') and ν_{20} (A'') modes have similar frequencies, which are close to the excitation energy of peak B. While peak B should be assigned to 14^1 because the ν_{20} mode is symmetry-forbidden, its non-FC behavior suggests that it may also have contributions from the ν_{20} mode. Peaks J and K are due to combinational vibrational levels of the 2-CNPyrr neutral.

4.2. The Photodetachment Spectrum and Comparison with the Nonresonant PES. The PD spectrum shown in Figure 4 contains rich spectroscopic and electronic information about 2-CNPyrr⁻ and the DBS. The below-threshold peak 0 indicates the zero-point level of the DBS and defines the binding energy of the DBS as $240 \pm 5 \text{ cm}^{-1}$. The twenty-three Feshbach resonances (1–23) are due to single-photon excitations to vibrational levels of the DBS

followed by vibrationally induced autodetachment. The distinct threshold and the above-threshold continuum represent the cross sections of single-photon nonresonant PD processes, increasing with the photon energy as new detachment channels open. PE spectra obey the FC principle in cases where there is no strong vibronic coupling, as discussed above for the PE spectra of 2-CNPyrr⁻ (Figure 8). Since the diffuse dipole-bound electron does not change the structure of the neutral core, we have found that PD spectra often resemble the PE spectra to some extent,²⁶ which is valuable for spectral assignments. The PE spectrum of 2-CNPyrr⁻ at 373.47 nm (Figure 3c), red-shifted by 240 cm^{-1} , is overlaid on the PD spectrum in Figure 9 by aligning the 0_0^0 transition to peak 0 of the PDS. It can be seen that major peaks of the PD spectra agree with the resolved vibrational peaks in the PE spectrum. Specifically, peaks A–K in the PE spectrum correspond to peaks 2, 4, 7–9, 11–13, and 16–18 in the PD spectrum, respectively. Additional weak peaks are observed in

Table 2. BEs of the Observed Vibrational Peaks in the PE Spectra of 2-CNPy⁻, Their Shifts from the 0-0 Transition, and Assignments. The Theoretical Frequencies (Table S1) of the Relevant Vibrational Modes of 2-CNPy Are Given for Comparison

peak	BE ^a (eV)	BE ^a (cm ⁻¹)	shift (cm ⁻¹)	assignment	calculation ^b (cm ⁻¹)
0 ₀ ⁰	3.0981(6)	24 988(5)	0		
A	3.1675(6)	25 548(5)	560	15 ¹	563
B	3.1889(6)	25 720(5)	732	20 ¹ /14 ¹	739/725
C	3.2095(8)	25 886(6)	898	13 ¹	894
D	3.2158(9)	25 937(7)	949	12 ¹	943
E	3.2275(8)	26 032(6)	1044	11 ¹	1039
F	3.2448(10)	26 171(8)	1183	9 ¹	1180
G	3.2580(12)	26 278(10)	1290	8 ¹	1285
H	3.2663(8)	26 344(6)	1356	6 ¹	1376
I	3.2860(10)	26 503(8)	1515	5 ¹	1510
J	3.3004(10)	26 620(8)	1632	14 ¹ 13 ¹	1619
K	3.3075(8)	26 677(6)	1689	14 ¹ 12 ¹	1668
a	3.1165(8)	25 136(6)	148	24 ¹	149
b	3.1193(10)	25 159(8)	171	17 ¹	173
c	3.1346(6)	25 282(5)	294	24 ²	298
d	3.1377(8)	25 307(6)	319	24 ¹ 17 ¹	322
e	3.1413(18)	25 336(15)	348	17 ²	346
f	3.1494(9)	25 402(7)	414	23 ¹	418
g	3.1622(8)	25 505(6)	517	22 ¹ /16 ¹	513/521
h	3.1783(8)	25 635(8)	647	21 ¹	656
i	3.1834(10)	25 676(10)	688	22 ¹ 17 ¹ / 17 ¹ 16 ¹	686/694
j	3.2010(10)	25 818(10)	830	19 ¹ /23 ²	841/836
k	3.2189(18)	25 962(15)	974	23 ¹ 15 ¹	981
l	3.2330(12)	26 076(10)	1088	10 ¹	1071
m	3.2485(8)	26 201(6)	1213	21 ¹ 15 ¹	1219
n	3.2532(6)	26 239(5)	1251	16 ¹ 14 ¹ / 16 ¹ 20 ¹	1246/1260
o	3.2565(12)	26 265(10)	1277	15 ¹ 14 ¹ / 15 ¹ 20 ¹	1288/1302
p	3.2739(6)	26 406(5)	1418	16 ¹ 13 ¹ / 22 ¹ 13 ¹	1415/1407
q	3.2795(12)	26 451(10)	1463	14 ² /20 ²	1450/1478
r	3.2907(6)	26 541(5)	1553	22 ³ /16 ³	1539/1563

^aNumbers in parentheses indicate the experimental uncertainties in the last digit. ^bCalculated frequencies are scaled by a factor of 0.972.

Table 3. Anisotropy Parameters for the Observed Vibrational Peaks in the Nonresonant PE Spectra at 373.47 nm (3.3198 eV, 26 776 cm⁻¹) with Their Corresponding Kinetic Energies

peak	KE, eV	KE, cm ⁻¹	β value ^a
0 ₀ ⁰	0.2217	1788	-0.45
A	0.1523	1228	-0.35
B	0.1309	1056	-0.40
C	0.1103	890	-0.45
D	0.104	839	-0.40
E	0.0923	744	-0.35
F	0.0750	605	-0.35
G	0.0618	498	-0.20
H	0.0538	432	-0.20
I	0.0338	273	-0.20
J	0.0194	156	-0.15
K	0.0123	99	-0.10

^aThe uncertainty of the β value is around ± 0.05 .

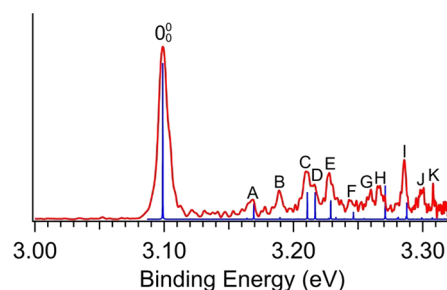


Figure 8. Comparison between the calculated FC factors and the nonresonant PE spectrum at 373.47 nm (3.3198 eV) from Figure 3c. The theoretical frequencies are scaled by a factor of 0.972.

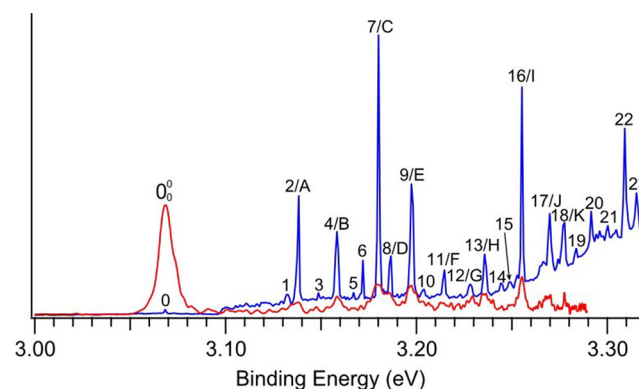


Figure 9. Comparison of the PE spectrum 373.47 nm (red) with the photodetachment spectrum (blue). The PE spectrum is red-shifted by 240 cm⁻¹ (0.0298 eV) to align peak 0₀⁰ with peak 0 of the photodetachment spectrum.

the PD spectrum, such as peaks 1, 3, 5, etc., that do not have corresponding features in the PE spectrum, demonstrating the high sensitivity of resonant excitations in the PDS. These additional transitions in the PD spectrum often yield new vibrational information about the neutral final state and are one of the reasons that PDS in conjunction with rPES can yield much richer spectroscopic information than conventional PES.²⁶ According to the assignments of peaks A–K in the PE spectra (Figure 8, Table 2), the corresponding Feshbach resonances in the PDS can be directly assigned to the same levels of the DBS. For example, peak 2 (15¹, Table 2) is assigned to 15¹ of the DBS (the prime (') is used to denote vibrational levels or modes of the DBS). Other PDS peaks can be similarly assigned according to the PES vibrational assignments in Table 2. However, there are still some significant differences between the PD spectrum and the PE spectra. In addition to the extra PD peaks, the relative intensities of the PD spectrum are not the same as the corresponding PES peaks, suggesting that some of the PDS peaks may contain transitions to multiple vibrational levels of the DBS with similar excitation energies. The nature and assignments of these extra PDS features can be investigated by rPES assisted by the $\Delta v = -1$ autodetachment propensity rules, yielding unprecedented spectroscopic information for the 2-CNPy radical.

4.3. R2PD Via the Bound Zero-Point Level of the DBS. R2PD–PEI of anions via below-threshold levels is powerful to characterize the nature of the DBS.^{10,62,63,71} The first R2PD–PEI via a DBS was performed for the phenoxide anion,¹⁰ revealing a distinct p-wave R2PD signal in agreement with the

σ -type dipole-bound orbital. The first π -type DBS was observed in the 9-anthrolate anion on the basis of a distinct ($s + d$)-wave R2PD PE image.⁶² Pump–Probe R2PD studies have been conducted to probe the lifetime and dynamics of the DBS in phenoxide.³³ As shown in Figure 5, the R2PD feature at the low BE side for 2-CNPyr[−] displays a beautiful p -wave angular distribution with a β value of 1.4, consistent with the σ -type DBS orbital as observed in previous studies. Since the dipole-bound electron has little influence on the corresponding neutral core, the dipole-bound anion and the neutral have identical geometries and parallel potential energy curves. Thus, photodetachment from the DBS to the neutral by the second photon is strictly adiabatic, namely, there is no change of vibrational energies from the DBS to the final neutral states. The adiabatic nature of electron detachment from the DBS has been demonstrated vividly by a single final state peak ($\nu_x' \rightarrow \nu_x$) for DBS vibrational levels in the phenylethynyl-phenoxide and anthryl-trifluoroethanolate anions^{71,72} as well as from PES of ground state dipole-bound anions.^{17,23}

The additional weak feature S_0 at the high BE side in Figure 5 is attributed to detachment from rovibrationally excited anions in the ground electronic state populated by relaxation from the DBS, because vibrational hot bands of 2-CNPyr[−] are fully eliminated in our cryogenically cooled ion trap. The binding energy of the S_0 feature is right at the detachment threshold, indicating that the rovibrational excitations in S_0 are slightly above 240 cm^{−1}, likely corresponding to rotational levels of the two lowest frequency modes ($\nu_{24} = 166$ cm^{−1} and $\nu_{17} = 186$ cm^{−1}, Figure S3). These rovibrationally excited anions are produced by relaxation from the zero-point level of the DBS following absorption of the first photon and then detached by a second photon within the same laser pulse of ~ 5 ns duration, as observed in the phenoxide anion and numerous other systems.^{10,63,72,73} The spectrum shown in Figure 5 is dominated by the direct R2PD process (the DBS peak), while the S_0 signal is very weak. This observation suggests that the coupling between the DBS and the ground electronic state of 2-CNPyr[−] is weak, resulting in a relatively long DBS lifetime.

4.4. Resonant Photoelectron Images and Spectra Via the Vibrational Feshbach Resonances. We obtained resonant PE images and spectra by tuning the detachment laser to the wavelength of each resonance, as shown in Figures 6 and 7. Two processes contribute to the total detachment cross section at the resonant wavelengths: the nonresonant direct detachment process and the resonantly enhanced vibrational autodetachment from the DBS. Because the diffuse dipole-bound electron has little effect on the structure of the neutral core, the geometry of the DBS and the corresponding neutral state are almost identical, resulting in the $\Delta v = -1$ propensity rule for the vibrational autodetachment process.^{24,25} For example, if a resonant excitation occurs to the DBS vibrational level ν_x^m (the n th quantum of the ν_x' mode), autodetachment will lead to the enhancement of the $(n-1)$ th level of the same vibrational mode in the neutral (ν_x^{n-1}). For autodetachment from a combinational level ($\nu_x^m \nu_x'^m \dots$) of the DBS, the final neutral state could be either $\nu_x^{m-1} \nu_x'^m \dots$ or $\nu_x^m \nu_x'^{m-1} \dots$, producing multiple enhanced vibrational peaks in rPES. Thus, one or more vibrational final states are enhanced in the resonant PE spectra, which are highly non-Franck–Condon compared with the nonresonant PE spectra in Figure 3. The autodetachment propensity rule can provide a valuable guide for spectral assignment, although violation of the $\Delta v = -1$ propensity rule can occur as a result of anharmonicity²⁴

and has been observed often for low-frequency bending modes.⁷⁴ For excitations to combinational or overlapping vibrational levels of the DBS, the resulting resonant PE spectra can be quite complicated, containing rich vibrational information that would not be assessable in nonresonant PES. Using the autodetachment propensity rule and the calculated vibrational frequencies of 2-CNPyr (Table S1), we are able to assign all the vibrational levels of the DBS and those observed in the resonant and nonresonant PE spectra.

4.4.1. Excitation to Fundamental Vibrational Levels of the DBS. According to the $\Delta v = -1$ propensity rule, excitation to fundamental vibrational levels of the DBS (ν_x^1) leads to the enhancement of the 0–0 transition (ν_x^0), such as that observed in the resonant PE spectra at peak 1 (Figure 6a) and peak 3 (Figure 6c). The enhanced 0–0 transition due to autodetachment can also be inferred by the more isotropic angular distribution, in contrast to the $s + d$ angular distribution observed for direct detachment. By comparing the excitation energies of peak 1 (514 cm^{−1}) and peak 3 (645 cm^{−1}) with the theoretical frequencies (Table S1), we can readily assign peak 1 to 16^1 (A' symmetry) or 22^1 (A'') of the DBS, which have similar frequencies, and peak 3 to 21^1 (A''). In principle, only in-plane vibrational modes with A' symmetry are FC-allowed for the planar molecule with C_s geometry. Vibrational modes of A'' symmetry may be observed due to vibronic coupling. Both peaks 1 and 3 are extremely weak in the PD spectrum (Figure 4); their observation was entirely due to the high sensitivity of PDS. In addition to the similar frequencies of the ν_{16}' (A') and ν_{22}' (A'') pair, the theoretical frequencies for modes ν_{14}' (A') and ν_{20}' (A'') are also close (Table S1). Considering the low detachment cross sections involving the out-of-plane vibrational modes, we only include the vibrational levels with the A' symmetry in cases where both are possible. Vibrational modes with the A'' symmetry are observed, for example, 21^1 (Figure 6c), $23^1 13^1$ (Figure 6l), $23^1 11^1$ (Figure 7c), and $21^1 7^1$ (Figure 7k), etc.

Similarly, since only the 0_0^0 peak is enhanced in the resonant PE spectrum in Figure 6k, peak 11 is assigned to 9^1 , consistent with the aligned peak F (9^1) in the nonresonant PE spectrum (Figure 9 and Table 2). Peak 7, which has the strongest intensity corresponds to C (13^1) in the nonresonant PE spectrum (Figure 9), which has the largest FC factor other than the 0–0 transition (Figure 3). Thus, peak 7 in the PD spectrum is assigned to 13^1 of the DBS, resulting in the enhanced 0_0^0 transition in Figure 6g. However, a very weak new peak (labeled *a*) with an excitation energy of 148 cm^{−1} is also discernible in Figure 6g, due to the lowest out-of-plane bending mode ν_{24}' of the DBS. The appearance of this low-frequency bending mode is likely due to inelastic scattering between the outgoing photoelectron and the neutral core, as observed previously.⁷⁴ Because of the strong excitation cross section for the ν_{13}' mode, its overtone $13^{1/2}$ is also observed (peak 20, Table 1), resulting in a single enhanced 13^1 transition in the resonant PE spectrum (peak C in Figure 7h).

Besides peaks 1, 3, 7, and 11 in the PD spectrum, peaks 2, 4, 8, 9, 12, 13, and 16 (Figure 4) should also include contributions from excitation to a fundamental vibrational level of the DBS, because all these DBS levels correspond to a fundamental excitation in the nonresonant PE spectrum (Figure 9, Table 2). In all these cases, there are overlapping excitations to other DBS vibrational levels, as revealed by the more complicated corresponding resonant PE spectra. In most cases, the enhanced 0_0^0 transition can also be glimpsed from

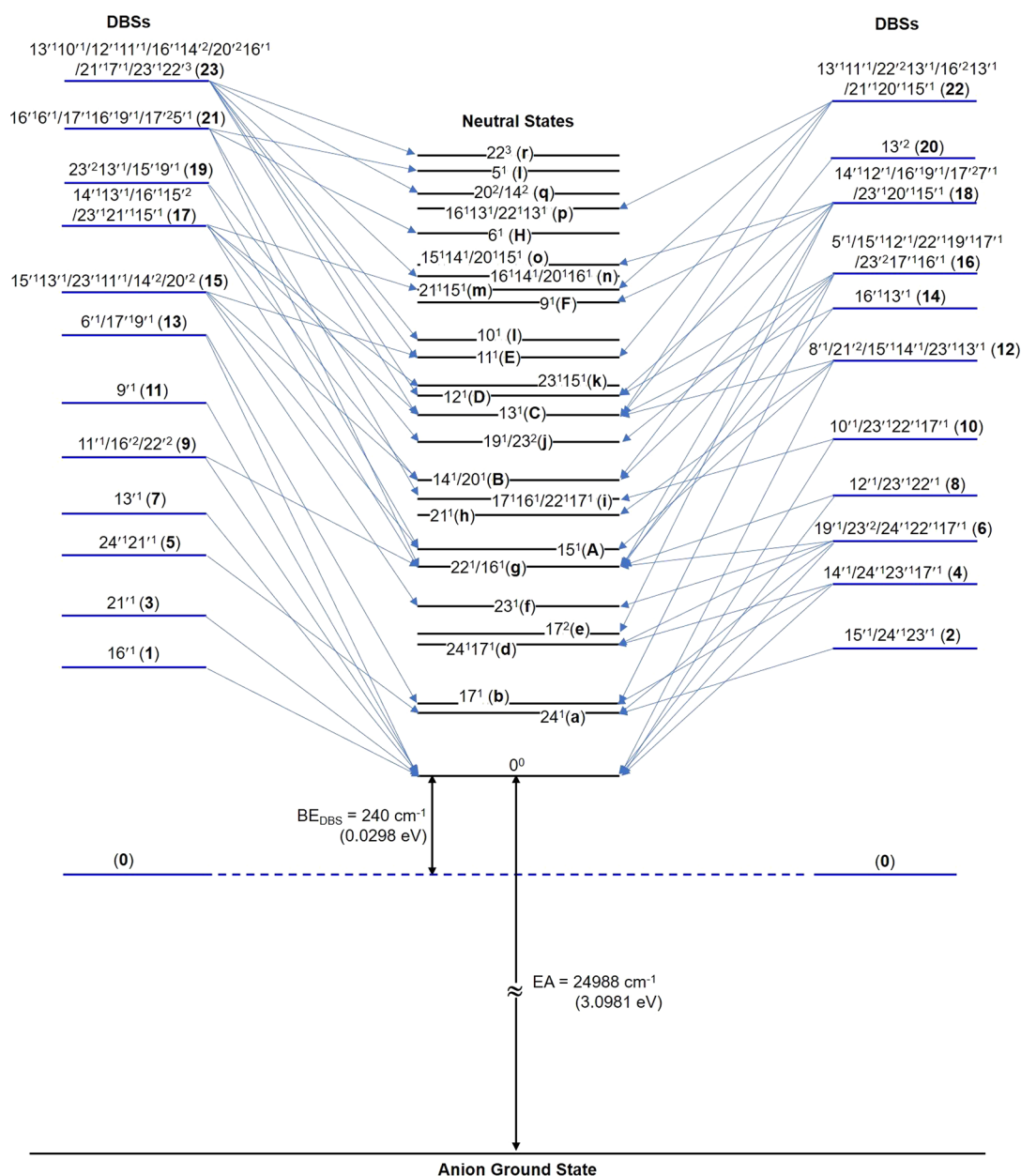


Figure 10. Schematic energy-level diagram for autodetachment from the DBS vibrational levels of 2-CNPyr⁻ to the neutral final states, corresponding to the 23 resonant PE spectra shown in Figures 6 and 7.

the more isotropic angular distributions. Peak 6 and peak 10 do not have corresponding transitions in the nonresonant PE spectrum (Figure 9), but the resonant PE spectra, Figure 6f at peak 6 and Figure 6j at peak 10, clearly display enhanced 0₀⁰ transitions, due to excitations to 19¹ and 10¹ of the DBS, respectively, along with other overlapping combinational levels.

4.4.2. Excitation to Combinational and Overlapping Levels of the DBS. Besides the 0₀⁰ transition, additional vibrational peaks are also enhanced in most of the resonant PE spectra (labeled in bold face in Figures 6 and 7) or new peaks have appeared (labeled in lowercase letters), which are generally from autodetachment of combinational and/or overlapping levels of the DBSs. For example, peak 2 in the PD spectrum must contain excitations to DBS level 15¹ as well as the combinational level 24¹23¹ (Figure 6b). The latter results in the appearance of a new peak *a* (24¹) with the vibrational energy of 23¹ coupled to the dipole-bound electron

for autodetachment. Note that one quantum of ν_{24}' is not enough to induce autodetachment because the vibrational energy is less than the binding energy of the dipole-bound electron. The excitation energy of peak *c* is 294 cm⁻¹, which can only be assigned to the overtone of ν_{24} (24²). However, peak 2 in the PD spectrum is 564 cm⁻¹ above the dipole-bound ground state, and it cannot be assigned to any combination of 24² and another mode with an excitation energy of 270 cm⁻¹. Most likely, peak *c* is due to vibronic coupling enhanced near threshold, as recently observed in a high-resolution PEI study of NiO₂⁻⁷⁵.

Besides the fundamental level 14¹, peak 4 in the PD spectrum must contain an overlapping DBS level of 24¹23¹17¹, resulting in the new peak *d* (24¹17¹) in the resonant PE spectrum (Figure 4d). The appearance of peak *b* (17¹) indicates a violation of the $\Delta\nu = -1$ propensity rule because two vibrational quanta 24¹23¹ must be coupled to

the dipole-bound electron. Similar violations are also observed in resonant PE spectra at other DBS levels, such as peak 6 (Figure 6f), peak 16 (Figure 7d), peak 17 (Figure 7e), peak 22 (Figure 7j), and peak 23 (Figure 7k). In many cases, multiple overlapping DBS levels are possible. For example, peak 6 is due to the overlap of three levels, $19^1/23^2/24^122^117^1$ (Figure 6f). The appearance of peak *d* (24^117^1) obeys the $\Delta v = -1$ propensity rule, whereas that of peaks *a* (24^1) and *g* (22^1) is caused by the violation of the propensity rule. The new peak *f* (23^1) is due to autodetachment from the 23^2 level of the DBS. Excitations to overlapping overtone levels of the DBS are also found in peak 9 (Figure 6i), peak 12 (Figure 6l), and peak 15 (Figure 7c).

With the increase of excitation energies and the increase of the vibrational density of states, more complicated resonant PE spectra are observed due to multiple overlapping DBS levels. These data, in turn, illustrate the power of rPES for providing much richer vibrational information for the neutral final states. The assignments of all the vibrational Feshbach resonances are summarized in Table 1, and the assignments of the PE final states are given in Table 2. The autodetachment processes from all the 23 Feshbach resonances are presented schematically in Figure 10.

4.4.3. Observation of a Resonantly-Enhanced Hot Band.

Surprisingly, a very weak but discernible peak, labeled as α , is observed in the spectrum of the weak Feshbach resonance peak 5 at a binding energy of 3.0850(15) eV or 24 882(12) cm^{-1} , which is 106 cm^{-1} lower than the 0–0 transition (3.0981 eV or 24 988 cm^{-1}). The peak below the 0–0 transition could only come from a vibrational hot band of the anion. According to the calculated frequencies of 2-CNPyr (Table S1) and 2-CNPyr⁻ (Table 2), we found that peak α is due to excitation from 23_a^1 (subscript *a* is used here to label the vibrational level of the anion in the ground electronic state) to the 23^113^1 DBS level, followed by autodetachment to 23^1 of the neutral, as shown in Figure 11. The frequency of mode ν_{23} of 2-CNPyr⁻ is measured to be 520(12) cm^{-1} , in good agreement with the calculated value of 521 cm^{-1} (Table S2). In principle, vibrational hot bands should be fully eliminated in our cryogenic ion trap, as confirmed by the nonresonant PE spectra in Figure 3. No hot bands even for the lowest frequency mode ν_{24} are observable. Apparently, the observation of the weak peak α is due to two factors. First, the $23_a^1 \rightarrow 23^113^1$ transition happens to coincide with the 24^121^1 Feshbach resonance. In fact, peak 5 is already the weakest Feshbach resonance in the PD spectrum (Figure 4), and the hot band transition only makes a minute contribution to this weak resonant peak. Second, the hot band transition involves a combination level with mode ν_{13} , which is the strongest peak in the PD spectrum. Thus, the observation of the resonantly enhanced peak α is completely accidental: the $23_a^1 \rightarrow 23^113^1$ hot band transition would be negligible if it were not coinciding with the 24^121^1 resonance. This accidental observation allowed us to obtain the experimental vibrational frequency for the ν_{23} mode of the anion.

4.4.4. Vibrational Information about the 2-CNPyr Radical.

Combining the PDS and rPES, we are able to measure the fundamental frequencies of 19 vibrational modes for the 2-CNPyr radical and one vibrational frequency for the 2-CNPyr⁻ anion, as summarized in Table 4. Vibrational frequencies are obtained for 13 modes with *A'* symmetry and six modes with *A''* symmetry for the 2-CNPyr radical among a total of 24 modes (Figure S2). The only vibrational modes of the 2-

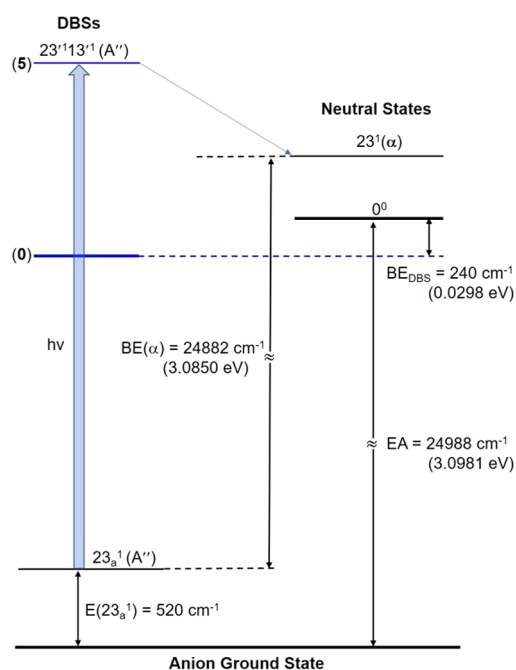


Figure 11. Schematic energy-level diagram showing the resonantly enhanced hot band transition to the 23^113^1 DBS level and the production of peak α following autodetachment.

Table 4. Measured Vibrational Frequencies for the 2-CNPyr Radical and the 2-CNPyr⁻ Anion in This Work, Compared with the Theoretical Values at the B3LYP/aug-cc-pVTZ Level of Theory

vibrational mode	symmetry	experimental frequency ^a (cm^{-1})	theoretical frequency ^b (cm^{-1})
ν_5	<i>A'</i>	1515(8)	1510
ν_6		1356(6)	1376
ν_7		1342(8)	1334
ν_8		1290(10)	1285
ν_9		1183(8)	1180
ν_{10}		1088(10)	1071
ν_{11}		1044(6)	1039
ν_{12}		949(7)	943
ν_{13}		898(6)	894
ν_{14}		732(5) ^c	725
ν_{15}		560(5)	563
ν_{16}		517(6) ^d	521
ν_{17}		171(8)	173
ν_{19}	<i>A''</i>	830(10)	841
ν_{20}		732(5) ^c	739
ν_{21}		647(8)	656
ν_{22}		517(6) ^d	513
ν_{23}		414(7)	418
ν_{24}		148(6)	149
ν_{23} (anion)	<i>A''</i>	520(12)	521

^aNumbers in parentheses indicate the experimental uncertainties in the last digit. ^bScaling factor 0.972. ^cThe frequencies of these two modes could not be distinguished experimentally. ^dThe frequencies of these two modes could not be distinguished experimentally.

CNPyr radical that are not observed are ν_{18} (*A''*) and the four high-frequency modes involving C–H stretching (ν_1 – ν_3) and the C–N stretching (ν_4). Frequencies of all other vibrational modes are measured directly or derived from the combination levels. In contrast, the conventional high-resolution PES

data presented in Figure 3 only yield vibrational frequencies for nine vibrational modes of A' symmetry (Table 2), demonstrating again the power of rPES via DBS to obtain vibrational spectroscopic information about polar radical species. This vibrational information should be valuable for the search and identification of the 2-CNPyr radical both in astronomical or combustion environments.

5. CONCLUSION

We report a high-resolution photoelectron imaging, photo-detachment spectroscopy, and resonant photoelectron imaging study of cryogenically cooled 2-CNPyr⁻ anions. The electron affinity of the 2-CNPyr radical is measured to be 3.0981 ± 0.0006 eV ($24\,988 \pm 5$ cm⁻¹). Strong vibronic coupling is observed between the ground electronic state of the 2-CNPyr radical and its first electronic excited state. A dipole-bound state is found for 2-CNPyr⁻ at 240 cm⁻¹ below the detachment threshold using photodetachment spectroscopy. Resonant two-photon detachment via the bound zero-point level of the DBS reveals that it has a relatively long lifetime. The photodetachment spectrum also exhibits a distinct s partial wave behavior near the detachment threshold of 2-CNPyr⁻ as well as 23 vibrational Feshbach resonances of the DBS. Highly non-Franck-Condon resonant photoelectron spectra are acquired at the vibrational Feshbach resonances, yielding rich vibrational information for the 2-CNPyr radical. Frequencies for 19 vibrational modes of the 2-CNPyr radical out of a total of 24 modes are measured, including 13 in-plane (A') and six out-of-plane (A'') vibrational modes.

■ ASSOCIATED CONTENT

Supporting Information

The Supporting Information is available free of charge at <https://pubs.acs.org/doi/10.1021/acs.jpca.2c04405>.

The schematic of the experimental apparatus, computed vibrational frequencies and atomic displacement vectors of the normal modes for the 2-cyanopyrrolyl neutral radical and 2-cyanopyrrolide anion (PDF)

■ AUTHOR INFORMATION

Corresponding Author

Lai-Sheng Wang – Department of Chemistry, Brown University, Providence, Rhode Island 02912, United States; orcid.org/0000-0003-1816-5738; Email: Lai-Sheng_Wang@brown.edu

Authors

Dao-Fu Yuan – Department of Chemistry, Brown University, Providence, Rhode Island 02912, United States; orcid.org/0000-0001-8461-6889

Yue-Rou Zhang – Department of Chemistry, Brown University, Providence, Rhode Island 02912, United States

Complete contact information is available at: <https://pubs.acs.org/doi/10.1021/acs.jpca.2c04405>

Notes

The authors declare no competing financial interest.

■ ACKNOWLEDGMENTS

This work was supported by the Department of Energy, Office of Basic Energy Sciences, Chemical Sciences, Geosciences, and Biosciences Division under Grant No. DE-SC0018679. The

calculation was performed using computational resources and services provided by CCV of Brown University.

■ REFERENCES

- (1) Simons, J. *Molecular Anions*. *J. Phys. Chem. A* **2008**, *112*, 6401–6511.
- (2) Jackson, R. L.; Zimmerman, A. H.; Brauman, J. I. Resonant States at Threshold Observed in Electron Photodetachment Cross Sections of Polyatomic Negative Ions. *J. Chem. Phys.* **1979**, *71*, 2088–2094.
- (3) Jackson, R. L.; Hiberty, P. C.; Brauman, J. I. Threshold Resonances in the Electron Photodetachment Spectrum of Acetaldehyde Enolate Anion. Evidence for a Low-Lying, Dipole-Supported State. *J. Chem. Phys.* **1981**, *74*, 3705–3712.
- (4) Marks, J.; Comita, P. B.; Brauman, J. I. Threshold Resonances in Electron Photodetachment Spectra. Structural Evidence for Dipole-Supported States. *J. Am. Chem. Soc.* **1985**, *107*, 3718–3719.
- (5) Mead, R. D.; Lykke, K. R.; Lineberger, W. C.; Marks, J.; Brauman, J. I. Spectroscopy and Dynamics of the Dipole-bound State of Acetaldehyde Enolate. *J. Chem. Phys.* **1984**, *81*, 4883–4892.
- (6) Lykke, K. R.; Mead, R. D.; Lineberger, W. C. Observation of Dipole-Bound States of Negative Ions. *Phys. Rev. Lett.* **1984**, *52*, 2221–2224.
- (7) Andersen, T.; Lykke, K. R.; Neumark, D. M.; Lineberger, W. C. Autodetachment Study of the Electronic Spectroscopy of FeO⁻. *J. Chem. Phys.* **1987**, *86*, 1858–1867.
- (8) Yokoyama, K.; Leach, G. W.; Kim, J. B.; Lineberger, W. C.; Boldyrev, A. I.; Gutowski, M. Autodetachment Spectroscopy and Dynamics of Vibrationally Excited Dipole-bound States of H₂CCC⁻. *J. Chem. Phys.* **1996**, *105*, 10706–10718.
- (9) Dessent, C. E. H.; Kim, J.; Johnson, M. A. Photochemistry of Halide Ion-Molecule Clusters: Dipole-Bound Excited States and the Case for Asymmetric Solvation. *Acc. Chem. Res.* **1998**, *31*, 527–534.
- (10) Liu, H. T.; Ning, C. G.; Huang, D. L.; Dau, P. D.; Wang, L. S. Observation of Mode-Specific Vibrational Autodetachment from Dipole-Bound States of Cold Anions. *Angew. Chem., Int. Ed.* **2013**, *52*, 8976–8979.
- (11) Liu, H. T.; Ning, C. G.; Huang, D. L.; Wang, L. S. Vibrational Spectroscopy of the Dehydrogenated Uracil Radical via Autodetachment of Dipole-Bound Excited States of Cold Anions. *Angew. Chem., Int. Ed.* **2014**, *53*, 2464–2468.
- (12) Dao, D. B.; Mabbs, R. The Effect of the Dipole Bound State on AgF⁻ Vibrationally Resolved Photodetachment Cross Sections and Photoelectron Angular Distributions. *J. Chem. Phys.* **2014**, *141*, 154304.
- (13) Mascariolo, K. J.; Gardner, A. M.; Heaven, M. C. Autodetachment Spectroscopy of the Aluminum Oxide Anion Dipole Bound State. *J. Chem. Phys.* **2015**, *143*, 114311.
- (14) Castellani, M. E.; Anstoter, C. S.; Verlet, J. R. R. On the Stability of a Dipole-Bound State in the Presence of a Molecule. *Phys. Chem. Chem. Phys.* **2019**, *21*, 24286–24290.
- (15) Desfrancois, C.; Abdoulcarime, H.; Khelifa, N.; Schermann, J. P. From $1/r$ to $1/r^2$ Potentials - Electron-Exchange between Rydberg Atoms and Polar-Molecules. *Phys. Rev. Lett.* **1994**, *73*, 2436–2439.
- (16) Hammer, N. I.; Diri, K.; Jordan, K. D.; Desfrancois, C.; Compton, R. N. Dipole-Bound Anions of Carbonyl, Nitrile, and Sulfoxide Containing Molecules. *J. Chem. Phys.* **2003**, *119*, 3650–3660.
- (17) Hammer, N. I.; Hinde, R. J.; Compton, R. N.; Diri, K.; Jordan, K. D.; Radisic, D.; Stokes, S. T.; Bowen, K. H. Dipole-Bound Anions of Highly Polar Molecules: Ethylene Carbonate and Vinylene Carbonate. *J. Chem. Phys.* **2004**, *120*, 685–690.
- (18) Qian, C. H.; Zhu, G. Z.; Wang, L. S. Probing the Critical Dipole Moment to Support Excited Dipole-Bound States in Valence-Bound Anions. *J. Phys. Chem. Lett.* **2019**, *10*, 6472–6477.
- (19) Desfrancois, C.; Abdoul-Carmine, H.; Schermann, J. P. Ground-State Dipole-Bound Anions. *Int. J. Mod. Phys. B* **1996**, *10*, 1339–1395.

- (20) Compton, R. N.; Hammer, N. I. Multiple-Bound Molecular Anions. In *Advances in Gas-Phase Ion Chemistry*; Adams, N. G., Ed.; JAI: Greenwich, CT, 2001; Vol. 4, pp 257–305.
- (21) Jordan, K. D.; Wang, F. Theory of Dipole -Bound Anions. *Annu. Rev. Phys. Chem.* **2003**, *54*, 367–396.
- (22) Compton, R. N.; Carman, H. S.; Desfrancois, C.; Abdoul-Carime, H.; Schermann, J. P.; Hendricks, J. H.; Lyapustina, S. A.; Bowen, K. H. On the Binding of Electrons to Nitromethane: Dipole and Valence Bound Anions. *J. Chem. Phys.* **1996**, *105*, 3472–3478.
- (23) Ciborowski, S. M.; Liu, G.; Graham, J. D.; Buytendyk, A. M.; Bowen, K. H. Dipole-Bound Anions: Formed by Rydberg Electron Transfer (RET) and Studied by Velocity Map Imaging-Anion Photoelectron Spectroscopy (VMI-aPES). *Eur. Phys. J. D* **2018**, *72*, 139.
- (24) Berry, R. S. Ionization of Molecules at Low Energies. *J. Chem. Phys.* **1966**, *45*, 1228–1245.
- (25) Simons, J. Propensity Rules for Vibration-Induced Electron Detachment of Anions. *J. Am. Chem. Soc.* **1981**, *103*, 3971–3976.
- (26) Zhu, G. Z.; Wang, L. S. High-Resolution Photoelectron Imaging and Resonant Photoelectron Spectroscopy via Noncovalent-Bound Excited States of Cryogenically-Cooled Anions. *Chem. Sci.* **2019**, *10*, 9409–9423.
- (27) Huang, D. L.; Liu, H. T.; Ning, C. G.; Wang, L. S. Vibrational State-Selective Autodetachment Photoelectron Spectroscopy from Dipole-Bound States of Cold 2-Hydroxyphenoxide: $o\text{-HO}(\text{C}_6\text{H}_4)\text{O}^-$. *J. Chem. Phys.* **2015**, *142*, 124309.
- (28) Huang, D. L.; Liu, H. T.; Ning, C. G.; Zhu, G. Z.; Wang, L. S. Probing the Vibrational Spectroscopy of the Deprotonated Thymine Radical by Photodetachment and State-Selective Autodetachment Photoelectron Spectroscopy via Dipole-Bound States. *Chem. Sci.* **2015**, *6*, 3129–3138.
- (29) Zhu, G. Z.; Huang, D. H.; Wang, L. S. Conformation-Selective Resonant Photoelectron Imaging from Dipole-Bound States of Cold 3-Hydroxyphenoxide. *J. Chem. Phys.* **2017**, *147*, 013910.
- (30) Qian, C. H.; Zhang, Y. R.; Yuan, D. F.; Wang, L. S. Photodetachment Spectroscopy and Resonant Photoelectron Imaging of Cryogenically Cooled 1-Pyrenolate. *J. Chem. Phys.* **2021**, *154*, 094308.
- (31) Zhang, Y. R.; Yuan, D. F.; Wang, L. S. Observation of Core-Excited Dipole-Bound States. *J. Phys. Chem. Lett.* **2022**, *13*, 2124–2129.
- (32) Laws, B. A.; Levey, Z. D.; Schmidt, T. W.; Gibson, S. T. Velocity Map Imaging Spectroscopy of the Dipole-Bound State of CH_2CN^- : Implications for the Diffuse Interstellar Band. *J. Am. Chem. Soc.* **2021**, *143*, 18684–18692.
- (33) Kang, D. H.; An, S.; Kim, S. K. Real-Time Autodetachment Dynamics of Vibrational Feshbach Resonances in a Dipole-Bound State. *Phys. Rev. Lett.* **2020**, *125*, 093001.
- (34) Kang, D. H.; Kim, J.; Kim, S. K. Dynamic Role of the Correlation Effect Revealed in the Exceptionally Slow Autodetachment Rates of the Vibrational Feshbach Resonances in the Dipole-Bound State. *Chem. Sci.* **2022**, *13*, 2714–2720.
- (35) Zhang, Y. R.; Yuan, D. F.; Wang, L. S. Probing the Electronic Structure and Spectroscopy of the Pyrrolyl and Imidazolyl Radicals using High Resolution Photoelectron Imaging of Cryogenically-Cooled Anions. *Phys. Chem. Chem. Phys.* **2022**, *24*, 6505–6514.
- (36) Jackson, A. H.; Smith, K. M. In *The Total Synthesis of Natural Products*; ApSimon, J., Ed.; Wiley: New York, 1984; Vol. 6, pp 237–280.
- (37) Adamczyk, M.; Reddy, R. E. A New Methodology for the Preparation of 2-Cyanopyrroles and Synthesis of Porphobilinogen. *Tetrahedron* **1996**, *52*, 14689–14700.
- (38) Adamczyk, M.; Reddy, R. E. A Convenient Synthesis of 2-Cyanopyrroles from Isocyanacetone. *Tetrahedron Lett.* **1995**, *36*, 7983–7986.
- (39) Zanatta, M.; Simon, N. M.; Dupont, J. The Nature of Carbon Dioxide in Bare Ionic Liquids. *ChemSusChem* **2020**, *13*, 3101–3109.
- (40) McKellar, A. Evidence for the Molecular Origin of Some Hitherto Unidentified Interstellar Lines. *PASP* **1940**, *52*, 187.
- (41) Savage, C.; Apponi, A. J.; Ziurys, L. M.; Wyckoff, S. Galactic $^{12}\text{C}/^{13}\text{C}$ Ratios from Millimeter-Wave Observations of Interstellar CN. *ApJ* **2002**, *578*, 211.
- (42) Agúndez, M.; Cernicharo, J.; Guélin, M.; Kahane, C.; Roueff, E.; Klos, J.; Aoiz, F. J.; Lique, F.; Marcelino, N.; Goicoechea, J. R.; González García, M.; Gottlieb, C. A.; McCarthy, M. C.; Thaddeus, P. Astronomical Identification of CN^- , the Smallest Observed Molecular Anion. *A&A* **2010**, *517*, L2.
- (43) Vazart, F.; Latouche, C.; Skouteris, D.; Balucani, N.; Barone, V. Cyanomethanimine Isomers in Cold Interstellar Clouds: Insights from Electronic Structure and Kinetic Calculations. *ApJ* **2015**, *810*, 111.
- (44) Tonolo, F.; Lupi, J.; Puzzarini, C.; Barone, V. The Quest for a Plausible Formation Route of Formyl Cyanide in the Interstellar Medium: A State-of-the-Art Quantum-Chemical and Kinetic Approach. *ApJ* **2020**, *900*, 85.
- (45) Cooke, I. R.; Gupta, D.; Messinger, J. P.; Sims, I. R. Benzonitrile as a Proxy for Benzene in the Cold ISM: Low-Temperature Rate Coefficients for $\text{CN} + \text{C}_6\text{H}_6$. *ApJL* **2020**, *891*, L41.
- (46) Saito, S.; Yamamoto, S.; Irvine, W. M.; Ziurys, L. M.; Suzuki, H.; Ohishi, M.; Kaifu, N. Laboratory Detection of a New Interstellar Free Radical CH_2CN ($^2\text{B}_1$). *ApJ* **1988**, *334*, L113.
- (47) Irvine, W. M.; Friberg, P.; Hjalmarsen, A.; Ishikawa, S.; Kaifu, N.; Kawaguchi, K.; Madden, S. C.; Matthews, H. E.; Ohishi, M.; Saito, S.; Suzuki, H.; Thaddeus, P.; Turner, B. E.; Yamamoto, S.; Ziurys, L. M. Identification of the Interstellar Cyanomethyl Radical (CH_2CN) in the Molecular Clouds TMC-1 and Sagittarius B2. *ApJ* **1988**, *334*, L107.
- (48) McCarthy, M. C.; Lee, K. L. K.; Loomis, R. A.; Burkhardt, A. M.; Shingledecker, C. N.; Charnley, S. B.; Cordiner, M. A.; Herbst, E.; Kalenskii, S.; Willis, E. R.; Xue, C.; Remijan, A. J.; McGuire, B. A. Interstellar Detection of the Highly Polar Five-Membered Ring Cyanocyclopentadiene. *Nat. Astron.* **2021**, *5*, 176–180.
- (49) Lee, K. L. K.; Changala, P. B.; Loomis, R. A.; Burkhardt, A. M.; Xue, C.; Cordiner, M. A.; Charnley, S. B.; McCarthy, M. C.; McGuire, B. A. Interstellar Detection of 2-Cyanocyclopentadiene, $\text{C}_5\text{H}_3\text{CN}$, a Second Five-Membered Ring toward TMC-1. *ApJL* **2021**, *910*, L2.
- (50) McGuire, B. A.; Burkhardt, A. M.; Kalenskii, S.; Shingledecker, C. N.; Remijan, A. J.; Herbst, E.; McCarthy, M. C. Detection of the Aromatic Molecule Benzonitrile ($c\text{-C}_6\text{H}_5\text{CN}$) in the Interstellar Medium. *Science* **2018**, *359*, 202–205.
- (51) McGuire, B. A.; Loomis, R. A.; Burkhardt, A. M.; Lee, K. L. K.; Shingledecker, C. N.; Charnley, S. B.; Cooke, I. R.; Cordiner, M. A.; Herbst, E.; Kalenskii, S.; Siebert, M. A.; Willis, E. R.; Xue, C.; Remijan, A. J.; McCarthy, M. C. Detection of Two Interstellar Polycyclic Aromatic Hydrocarbons via Spectral Matched Filtering. *Science* **2021**, *371*, 1265–1269.
- (52) Chandler, D. W.; Houston, P. L. Two-dimensional Imaging of State-selected Photodissociation Products Detected by Multiphoton Ionization. *J. Chem. Phys.* **1987**, *87*, 1445–1447.
- (53) Helm, H.; Bjerre, N.; Dyer, M. J.; Huestis, D. L.; Saeed, M. Images of Photoelectrons Formed in Intense Laser Fields. *Phys. Rev. Lett.* **1993**, *70*, 3221–3224.
- (54) Pinare, J. C.; Baguenard, B.; Bordas, C.; Broyer, M. Photoelectron Imaging Spectroscopy of Small Clusters: Evidence for Non-Boltzmannian Kinetic-Energy Distribution in Thermionic Emission. *Phys. Rev. Lett.* **1998**, *81*, 2225–2228.
- (55) Eppink, A. T. J. B.; Parker, D. H. Velocity Map Imaging of Ions and Electrons Using Electrostatic Lenses: Application in Photoelectron and Photofragment Ion Imaging of Molecular Oxygen. *Rev. Sci. Instrum.* **1997**, *68*, 3477–3484.
- (56) Neumark, D. M. Slow Electron Velocity-Map Imaging of Negative Ions: Applications to Spectroscopy and Dynamics. *J. Phys. Chem. A* **2008**, *112*, 13287–13301.
- (57) Wang, L. S.; Ding, C. F.; Wang, X. B.; Barlow, S. E. Photodetachment Photoelectron Spectroscopy of Multiply Charged Anions Using Electrospray Ionization. *Rev. Sci. Instrum.* **1999**, *70*, 1957–1966.

- (58) Wang, X. B.; Wang, L. S. Development of a Low-Temperature Photoelectron Spectroscopy Instrument Using an Electrospray Ion Source and a Cryogenically Controlled Ion Trap. *Rev. Sci. Instrum.* **2008**, *79*, 073108.
- (59) León, I.; Yang, Z.; Liu, H. T.; Wang, L. S. The Design and Construction of a High-Resolution Velocity-Map Imaging Apparatus for Photoelectron Spectroscopy Studies of Size-Selected Clusters. *Rev. Sci. Instrum.* **2014**, *85*, 083106.
- (60) Wang, L. S. Electrospray Photoelectron Spectroscopy: From Multiply-Charged Anions to Ultracold Anions. *J. Chem. Phys.* **2015**, *143*, 040901.
- (61) Qian, C.-H.; Zhu, G.-Z.; Zhang, Y.-R.; Wang, L.-S. Photodetachment Spectroscopy and Resonant Photoelectron Imaging of the 2-Naphthoxide Anion via Dipole-Bound Excited States. *J. Chem. Phys.* **2020**, *152*, 214307.
- (62) Yuan, D. F.; Liu, Y.; Qian, C. H.; Zhang, Y. R.; Rubenstein, B. M.; Wang, L. S. Observation of a π -Type Dipole-Bound State in Molecular Anions. *Phys. Rev. Lett.* **2020**, *125*, 073003.
- (63) Yuan, D. F.; Zhang, Y. R.; Qian, C. H.; Liu, Y.; Wang, L. S. Probing the Dipole-Bound State in the 9-Phenanthrolate Anion by Photodetachment Spectroscopy, Resonant Two-Photon Photoelectron Imaging, and Resonant Photoelectron Spectroscopy. *J. Phys. Chem. A* **2021**, *125*, 2967–2976.
- (64) Garcia, G. A.; Nahon, L.; Powis, I. Two-Dimensional Charged Particle Image Inversion Using a Polar Basis Function Expansion. *Rev. Sci. Instrum.* **2004**, *75*, 4989–4996.
- (65) Dribinski, V.; Ossadtchi, A.; Mandelshtam, V. A.; Reisler, H. Reconstruction of Abel-Transformable Images: The Gaussian Basis-Set Expansion Abel Transform Method. *Rev. Sci. Instrum.* **2002**, *73*, 2634–2642.
- (66) Cooper, J.; Zare, R. N. Angular Distribution of Photoelectrons. *J. Chem. Phys.* **1968**, *48*, 942–943.
- (67) Frisch, M. J., Trucks, G. W., Schlegel, H. B., Scuseria, G. E., Robb, M. A., Cheeseman, J. R., Scalmani, G., Barone, V., Petersson, G. A., Nakatsujii, H., Li, X., Caricato, M., Marenich, A., Bloino, J., Janesko, B. G., Gomperts, R., Mennucci, B., Hratchian, H. P., Ortiz, J. V., Izmaylov, A. F., Sonnenberg, J. L., Williams-Young, D., Ding, F., Lipparini, F., Egidi, F., Goings, J., Peng, B., Petrone, A., Henderson, T., Ranasinghe, D., Zakrzewski, V. G., Gao, J., Rega, N., Zheng, G., Liang, W., Hada, M., Ehara, M., Toyota, K., Fukuda, R., Hasegawa, J., Ishida, M., Nakajima, T., Honda, Y., Kitao, O., Nakai, H., Vreven, T., Throssell, K., Montgomery, J. A., Jr.; Peralta, J. E., Ogliaro, F., Bearpark, M., Heyd, J. J., Brothers, E., Kudin, K. N., Staroverov, V. N., Keith, T., Kobayashi, R., Normand, J., Raghavachari, K., Rendell, A., Burant, J. C., Iyengar, S. S., Tomasi, J., Cossi, M., Millam, J. M., Klene, M., Adamo, C., Cammi, R., Ochterski, J. W., Martin, R. L., Morokuma, K., Farkas, O., Foresman, J. B.; Fox, D. J. *Gaussian 09*, rev. D.01; Gaussian, Inc.: Wallingford, CT, 2016.
- (68) Wigner, E. P. On the Behavior of Cross Sections Near Thresholds. *Phys. Rev.* **1948**, *73*, 1002–1009.
- (69) Motzke, A.; Lan, Z.; Woywod, C.; Domcke, W. Simulation of the Photodetachment Spectrum of the Pyrrolide Anion. *Chem. Phys.* **2006**, *329*, 50–64.
- (70) Zhu, X.; Yarkony, D. R. The Photoelectron Spectrum of Pyrrolide: Nonadiabatic Effects Due to Conical Intersections. *J. Phys. Chem. C* **2010**, *114*, 5312–5320.
- (71) Yuan, D. F.; Liu, Y.; Qian, C. H.; Kocheril, G. S.; Zhang, Y. R.; Rubenstein, B. M.; Wang, L. S. Polarization of Valence Orbitals by the Intramolecular Electric Field from a Diffuse Dipole-Bound Electron. *J. Phys. Chem. Lett.* **2020**, *11*, 7914–7919.
- (72) Zhu, G. Z.; Cheung, L. F.; Liu, Y.; Qian, C. H.; Wang, L. S. Resonant Two-Photon Photoelectron Imaging and Intersystem Crossing from Excited Dipole-Bound States of Cold Anions. *J. Phys. Chem. Lett.* **2019**, *10*, 4339–4344.
- (73) Zhang, Y. R.; Yuan, D. F.; Qian, C. H.; Wang, L. S. Observation of a Dipole-Bound Excited State in 4-Ethynylphenoxide and Comparison with the Quadrupole-Bound Excited State in the Isoelectronic 4-Cyanophenoxide. *J. Chem. Phys.* **2021**, *155*, 124305.
- (74) Huang, D. L.; Liu, H. T.; Ning, C. G.; Dau, P. D.; Wang, L. S. Resonant Photoelectron Imaging of Deprotonated Uracil Anion via Vibrational Levels of a Dipole-Bound Excited State. *Chem. Phys.* **2017**, *482*, 374–383.
- (75) Babin, M. C.; DeWitt, M.; Lau, J. A.; Weichman, M. L.; Kim, J. B.; Cheng, L.; Neumark, D. M. Photoelectron Spectroscopy of Cryogenically Cooled NiO_2^- via Slow Photoelectron Velocity-Map Imaging. *Phys. Chem. Chem. Phys.* **2022**, *24*, 17496–17503.

Recommended by ACS

Nonadiabatic Dynamics between Valence, Nonvalence, and Continuum Electronic States in a Heteropolycyclic Aromatic Hydrocarbon

James N. Bull, Jan R. R. Verlet, *et al.*

DECEMBER 06, 2021

THE JOURNAL OF PHYSICAL CHEMISTRY LETTERS

READ 

Observation of Transient Anions That Do Not Decay through Dissociative Electron Attachment: New Pathways for Radiosensitization

Ana I. Lozano, Gustavo García, *et al.*

JULY 27, 2022

THE JOURNAL OF PHYSICAL CHEMISTRY LETTERS

READ 

Toward Detection of FeH^+ in the Interstellar Medium: Infrared Multiple Photon Dissociation Spectroscopy of Ar_2FeH^+

Shan Jin, Martin K. Beyer, *et al.*

JUNE 21, 2022

THE JOURNAL OF PHYSICAL CHEMISTRY LETTERS

READ 

Temporary Anion Resonances of Pyrene: A 2D Photoelectron Imaging and Computational Study

Aude Lietard, Kenneth D. Jordan, *et al.*

AUGUST 09, 2021

THE JOURNAL OF PHYSICAL CHEMISTRY A

READ 

Get More Suggestions >